Chirped four-wave mixing

Koos Duppen, Foppe de Haan, Erik T. J. Nibbering, and Douwe A. Wiersma
Ultrafast Laser and Spectroscopy Laboratory, Materials Science Center, University of Groningen, Nijenborgh 4, 9747 AG Groningen, The Netherlands
(Received 29 December 1992)

We will demonstrate that four-wave mixing with linearly chirped (phase-modulated) pulses is a unique tool for obtaining information on the dynamics and level structure of a system. Especially, it will be shown that the transient-grating-scattering type of experiment with chirped pulses provides an immediate answer to the question of whether the dynamics of a system occurs on a fast and/or slow time scale. In addition, we present compelling evidence that chirped four-wave mixing in a molecular system is a viable method for measuring excited-state vibrational frequencies. Double-sided Feynman diagrams are used for a third-order perturbative calculation of two-level four-wave-mixing effects and chirped coherent Raman scattering. The diagrams provide a visual representation of the quantum-mechanical pathways that the system can take as a result of the different field interactions. The number of quantum-mechanical pathways that contribute to the signal is shown to depend on the chirp rate compared to the time scale(s) of the system dynamics. A stochastic model is used to describe the optical dynamics of the system. The resulting expressions for the third-order nonlinear polarization are so complex that numerical calculations are necessary to simulate the time dependence of the optical response. It will also be shown that our theoretical results in the appropriate limits converge to those obtained for impulsive or continuous-wave excitation.

PACS number(s): 42.50.Md, 78.47.+p, 42.65.Dr, 42.65.Re

I. INTRODUCTION

A chirped wave has a phase that varies nonlinearly with time, and hence its instantaneous frequency is time dependent as well. In nature, chirped acoustical waves are well known. Birds generate them to communicate among each other [1], and certain species of bats employ them for maneuvering in the dark, and to locate and track their prey [2]. Electromagnetic chirped pulses have been used for a long time in radar, to detect and guide airplanes and ships [3]. At optical frequencies chirped pulses are often formed spontaneously during the buildup of a pulse inside a laser cavity [4], in which case the chirp is not well defined.

By phase modulation of optical fields a chirp can be induced that is defined over the entire pulse envelope. This was originally accomplished by electro-optic modulation [5], and more recently by injection of the field in a monomode optical fiber [6]. It was soon realized that these phase-modulated, frequency-broadened pulses could be compressed in time to their Fourier-transform-limited width by passage through frequency-dispersive delay lines such as a pair of gratings [7] or an array of prisms [8]. However, it was not before full understanding was achieved of the chirp-forming process in single-mode fibers [9,10] that breakthroughs were made in femtosecond pulse generation [11] and long-distance communication [12]. Also, the amplification of ultrashort pulses to extremely high energies has benefited from the controlled chirping of pulses, in order to extract the energy in the amplifier medium most efficiently [13].

Recently, the potential of pulses with a controlled chirp was also recognized for laser chemistry [14,15], selective optical excitation [16,17], and the study of optical dynamics [18,19]. In the field of pulsed NMR it was shown that excitation with chirped pulses produces states that are not easily accessible with transform-limited pulses [20].

In this paper we demonstrate that linearly chirped optical pulses can be used advantageously in a study of the optical dynamics of a molecule in solution. These pulses, which may have a duration-bandwidth product that exceeds the transform limited value by orders of magnitude, excite the system in a unique way. We show that dynamical information can be obtained that is not available from experiments using continuous-wave or short-pulse excitation. Specifically, we show that transient-grating-scattering type experiments with chirped pulses provide an immediate answer to the question of whether or not the dynamics of the solvent can be separated into fast and slow fluctuations. If so, the optical Bloch equations can be used to describe the dynamics; if not, a non-Markovian master equation needs to be employed.

The main body of this paper is focused on numerical calculations of chirped four-wave-mixing effects based on third-order perturbation theory. A stochastic model is used to simulate the optical dynamics of the probe molecule. Double-sided Feynman diagrams provide a pictorial representation of the calculations, and act as an aid in the interpretation of the results obtained for the different limits of solvent dynamics. We further show that good agreement is obtained between the calculated response and the signals that were observed experimentally. A brief report of this work was recently published [19].

The experimental arrangement that we will treat explicitly is shown in Fig. 1. Two beams with wave vectors

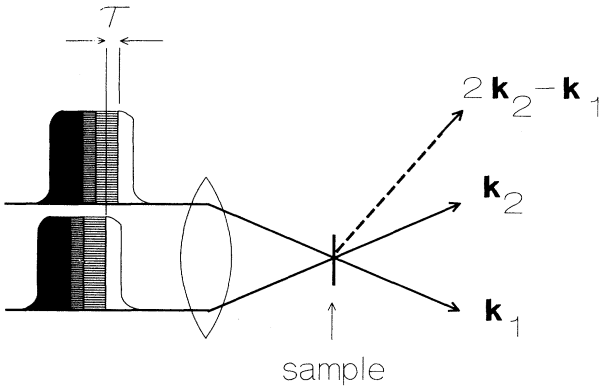

FIG. 1. Layout of the chirped nonlinear scattering experiment. Two pulses sweep through a system resonance and generate a signal in the direction $2\mathbf{k}_2-\mathbf{k}_1$. The integrated signal intensity is observed as a function of the relative delay τ, which is small compared to the pulse duration. The delay is associated with an instantaneous frequency difference between both beams. The object of this experiment is to obtain information on the dynamics of the system.

$\mathbf{k}_1$ and $\mathbf{k}_2$ interact in a sample and cause a signal to be emitted in the direction $\mathbf{k}_s=2\mathbf{k}_2-\mathbf{k}_1$. This is the general kind of geometry that has been used in impulsive scattering [21–24], steady-state interactions [25,26], with stochastic fields [27,28], and also in the first experiments with chirped laser pulses [18,19]. Figure 2 shows for a particular dye molecule in solution how the signal with chirped pulses depends on the relative delay between the two beams. The chirp was generated by focusing a 50-fs amplified colliding-pulse mode-locked (CPM) laser pulse in a monomode fiber. For comparison, the experimental result using short (9 fs) compressed pulses with the same frequency spectrum is also depicted.

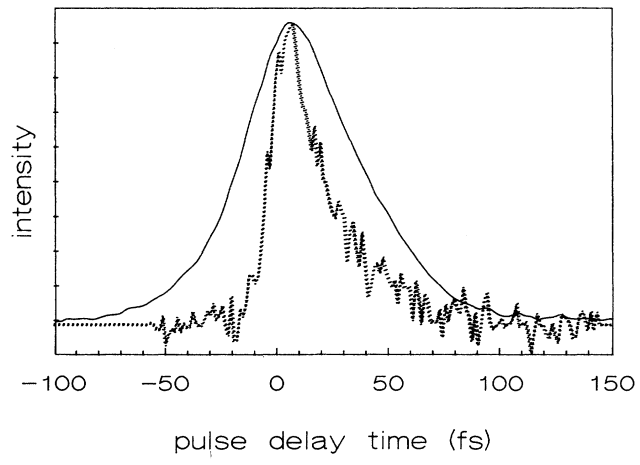

FIG. 2. Two-pulse delayed scattering signal at room temperature for the dye molecule resorufin dissolved in dimethylsulfoxide. The solid trace was obtained with chirped pulses. The pulse duration was about 1.5 ps with a chirp rate in angular frequency units of 0.5 THz/fs. The dotted trace was obtained when the pulses were compressed to a duration of 9 fs. In the compression process the phases of the frequency components are rearranged while the frequency spectrum is not influenced.

We will demonstrate that these results can be interpreted within a two-level model for the system dynamics. In addition, coherent Raman scattering signals are generated, from which ground- and excited-state vibrational frequencies can be obtained. The relative intensities of the Stokes and anti-Stokes signals depend on the direction of the chirp, i.e., whether the instantaneous frequency increases or decreases in time. "With femtosecond lasers becoming as ubiquitous as 5 Volt batteries" [29], it may well be that this relatively simple two-beam scattering experiment will become a routine technique for acquiring information on vibrational frequencies in the ground and excited states of molecules.

The paper is organized as follows: In the second section double-sided Feynman diagrams are introduced and used to calculate the third-order nonlinear response functions, adopting a stochastic relaxation model. In the third section the effect of linear chirp of the excitation fields is explicitly accounted for, and the limits of very fast and very slow chirp are examined. It is shown that for very fast chirp the impulsive excitation limit is reached, while for very slow chirp the connection with continuous-wave excitation is made. In the fourth section the numerical calculations of the nonlinear signals are presented. In particular it will be shown that the chirp rate in comparison with the time scale(s) of system dynamics is the crucial factor in determining the shape of the coherent signals. In Sec. V, chirped four-wave mixing in multilevel systems is examined, both experimentally and by calculations. Here the sign of the chirp parameter will be shown to have pronounced effects on the observed signal intensities. Finally, in Sec. VI our findings are summarized and some conclusions are drawn regarding the potential of chirped transient-grating-scattering experiments.

II. NONLINEAR RESPONSE THEORY

A. Four-wave mixing

The transient-grating-scattering process depicted in Fig. 1 can be seen as a member of a broad family of processes, known as four-wave mixing. The general four-wave-mixing process involves the interaction of three light fields with wave vectors $\mathbf{k}_1$, $\mathbf{k}_2$, and $\mathbf{k}_3$ and frequencies ω_1, ω_2, and ω_3 to generate a signal with wave vector $\mathbf{k}_s$ and frequency ω_s:

$$\mathbf{k}_s=\pm\mathbf{k}_1\pm\mathbf{k}_2\pm\mathbf{k}_3 , \tag{1a}$$

$$\omega_s=\pm\omega_1\pm\omega_2\pm\omega_3 . \tag{1b}$$

In the usual perturbative treatment of these processes the medium is assumed to be partly quantized and the electromagnetic fields are taken to be classical. The quantized system and optical fields interact through dipolar coupling, and the signal is generated through the nonlinear response of the system. In this section we will consider a two-level system, stochastically perturbed by bath

degrees of freedom that interact with the two-level system but not with the electromagnetic fields. The system Hamiltonian thus consists of two levels $|a\rangle$ and $|b\rangle$, dressed phenomenologically with parameters that describe damping and linewidth for ensemble-averaged properties.

A convenient way to include damping in a description of the system dynamics is to make use of the density-matrix formalism. The third-order nonlinear response of the material is calculated by considering three consecutive interactions between system and field. This then yields an ensemble-averaged nonlinear polarization according to

$$P(\mathbf{r},t)=\mathrm{Tr}\{\mu\rho(\mathbf{r},t)\}\equiv\langle\langle\mu|\rho(\mathbf{r},t)\rangle\rangle \ . \tag{2}$$

Here, μ is the dipole moment operator of the system and $\rho(\mathbf{r},t)$ is the reduced density operator of the system. For simplicity we take P and μ to be scalar quantities here. The density operator is calculated by propagating the system from a time at which the radiation field is not yet present (e.g., $t=-\infty$) to time $t=t$ after the three system-field interactions. For a two-level system at room temperature with a transition frequency much larger than kT the unperturbed state at $t=-\infty$ is the ground state $\rho(\mathbf{r},-\infty)=|a\rangle\langle a|$. The nonlinear polarization at time t then has the following general form [30–33]:

$$P(\mathbf{r},t)=(-i)^3\sum_{\substack{j,k,l=1\\ j\neq k\neq l}}^{3}\int_0^\infty dt_3\int_0^\infty dt_2\int_0^\infty dt_1\langle\langle\mu|G(t_3)L_{\mathrm{int},l}(\mathbf{r},t-t_3)G(t_2)L_{\mathrm{int},k}(\mathbf{r},t-t_3-t_2)$$
$$\times G(t_1)L_{\mathrm{int},j}(\mathbf{r},t-t_3-t_2-t_1)|\rho(\mathbf{r},-\infty)\rangle\rangle \ . \tag{3}$$

The meaning of this expression is as follows: starting at $t=-\infty$ three interactions $L_{\mathrm{int}}(\mathbf{r},t)$ occur between system and field at times $t-t_3-t_2-t_1$, $t-t_3-t_2$, and $t-t_3$. In the intervals t_1, t_2, and t_3 between the interactions the system evolves according to the Green's-function propagators $G(t)$, which gives rise to oscillations and decays of the density-matrix elements.

The three interactions between system and fields are represented by Liouville space operators (or super operators) defined by

$$L_{\mathrm{int},j}(\mathbf{r},t)\rho(t)\equiv[\mathcal{H}_{\mathrm{int},j}(\mathbf{r},t),\rho(t)] \ . \tag{4}$$

The interaction Hamiltonians can be expanded in the states of the two-level system, which yields in the dipole approximation

$$\mathcal{H}_{\mathrm{int},j}(\mathbf{r},t)=\frac{|\mu_{ab}|}{\hbar}E_j(\mathbf{r},t)(|a\rangle\langle b|+|b\rangle\langle a|) \ . \tag{5}$$

Here $|\mu_{ab}|$ is the magnitude of the transition dipole moment between states $|a\rangle$ and $|b\rangle$ and $E_j(\mathbf{r},t)$ is one of three applied classical electromagnetic fields, which we take to be plane waves:

$$E_j(\mathbf{r},t)=\tfrac{1}{2}[E_j(t)e^{i\mathbf{k}_j\cdot\mathbf{r}}+E_j^*(t)e^{-i\mathbf{k}_j\cdot\mathbf{r}}] \ . \tag{6}$$

The time dependence $E_j(t)$ will be specified further in Sec. III when chirped fields are introduced explicitly in the formalism [Eq. (17)].

The physics of Eqs. (3)–(6) can be conveniently displayed in the form of diagrams [30–33]. These diagrams provide direct insight into the time evolution of the system and therefore in the influence of damping processes on the outcome of the nonlinear optical experiment. Each diagram can be translated by straightforward computational rules into mathematical expressions that can be evaluated analytically or numerically. The details of this translation depend on the character of the interaction Hamiltonian, and on the model that is chosen for the system dynamics. We will now briefly describe which diagrams are relevant for the process of Fig. 1, in which the nonlinear polarization is induced with wave vector $2\mathbf{k}_2-\mathbf{k}_1$. Subsequently we introduce a general dynamical model that applies to a large variety of optical systems.

B. Double-sided Feynman diagrams

Since each $L_{\mathrm{int}}(\mathbf{r},t)$ represents a commutator [Eq. (4)], the interactions of Eq. (3) can work on the bra and on the ket sides of the density operator. With three such interactions that can work on both sides of the density operator there are $(2)^3=8$ different pathways from the unperturbed state at $t=-\infty$ to the final state at $t=t$. The emission of the signal field can also occur on the bra and ket sides of the density operator but since this leads to diagrams that are Hermitian conjugates of each other, only 8 independent pathways remain.

The three fields that induce the changes in the state of the system are not necessarily time ordered. So, in the most general case of four-wave mixing $3!=6$ possible permutations have to be considered in the time ordering of these fields. For the type of scattering displayed in Fig. 1, one of the fields acts twice so two interactions are not permutable. This leaves only $3!/2=3$ remaining time orderings. Thus, the total number of independent diagrams that represents the nonlinear optical scattering of interest is 8 (number of system pathways) $\times 3$ (number of time orderings of the fields).

Inspection of these diagrams enables one to reduce the number of significant contributions from 24 to 4. The reason is that 20 of the diagrams contain one or more antirotating interactions. In such interactions a transition from the ground state of the system to the excited state is accompanied by the emission of a photon, or a transition from the excited state to the ground state by the absorption of a photon. Since these types of terms will be highly oscillatory, the time integrations of Eq. (3)

cause their contribution to the signal to be very small. In the rotating wave approximation they are simply neglected so that only four independent contributions remain. The relevant diagrams are depicted in Fig. 3, where the following convention is used: the ω branches with a positive inclination toward and from the system propagators correspond to $E_j(t)e^{i\mathbf{k}_j\cdot\mathbf{r}}$ working, respectively, on the bra and ket sides of the density matrix, and similarly the ω branches with a negative slope correspond to $E_j^*(t)e^{-i\mathbf{k}_j\cdot\mathbf{r}}$.

To write down the mathematical expression for the nonlinear polarization that is symbolized by these diagrams, Eqs. (4)–(6) have to be inserted in Eq. (3) with the fields acting in the right time ordering. The result is

$$P(\mathbf{r},t,\tau)=(2i\hbar)^{-3}|\mu_{ab}|^4 e^{i(2\mathbf{k}_2-\mathbf{k}_1)\cdot\mathbf{r}} \times\int_0^\infty dt_3\int_0^\infty dt_2\int_0^\infty dt_1\{[R_{\mathrm{I}}(t_3,t_2,t_1)+R_{\mathrm{II}}(t_3,t_2,t_1)]E_2(t-\tau-t_3)E_2(t-\tau-t_3-t_2)E_1^*(t-t_3-t_2-t_1) +[R_{\mathrm{III}}(t_3,t_2,t_1)+R_{\mathrm{IV}}(t_3,t_2,t_1)]E_2(t-\tau-t_3)E_1^*(t-t_3-t_2)E_2(t-\tau-\tau_3-t_2-t_1)\} . \quad (7)$$

Here, τ is the delay time that is introduced between beams 1 and 2, as depicted in Fig. 1, and $R_{\mathrm{I-IV}}(t_3,t_2,t_1)$ are the time evolution functions that result from propagating the ensemble of systems during times t_1, t_2, and t_3 according to diagrams I–IV. These functions are determined by the propagators $G(t_i)$ of Eq. (3), which in turn depend on the model that is adopted for the system-bath interaction.

C. The stochastic model of optical dynamics

In the intervals between the interactions of the system with the optical fields, the dynamics is governed by the energies ε_a and ε_b of the two-level system. Both of these energies are not completely defined due to population relaxation processes and fluctuations in the interactions between the system and its environment (the "bath"). It is often assumed that the time scales of system and bath dynamics are completely different, leading to homogeneous or inhomogeneous broadening of the transition frequency in the limits of much faster and more slower bath dynamics, respectively. In more general treatments of optical dynamics (non-Markovian approaches) this assumption is not made, which leads to memory effects in the propagation of the system under the influence of the bath. The future of the system then depends not only on the present but also on the evolution in the past. In this way any situation in between the limits of homogeneous and inhomogeneous broadening can be described.

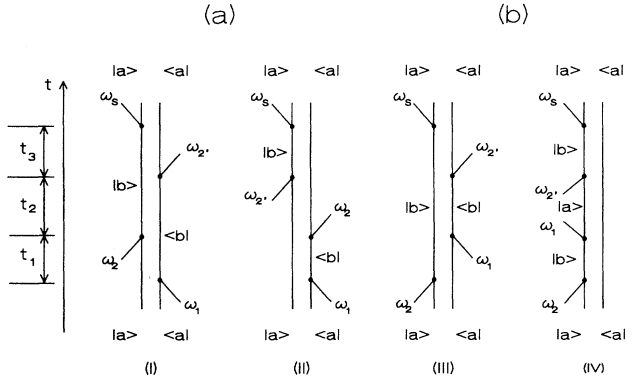

FIG. 3. Double-sided Feynman diagrams for resonance four-wave mixing in a two-level system. The two lines of each diagram represent the bra and ket sides of the density matrix. Time increases from bottom to top. The interactions between system and radiation field are represented by vertices. The signal is generated with wave vector $\mathbf{k}_s=2\mathbf{k}_2-\mathbf{k}_1$ and frequency $\omega_s=\omega_2'+\omega_2-\omega_1$. With phase-modulated pulses the instantaneous frequency is a function of time, so that frequency ω_2' is not necessarily identical to frequency ω_2. In diagrams (a) a superposition state of the system is inverted; in diagrams (b) the same superposition state occurs twice.

A model that applies to system-bath dynamics on arbitrary time scales is the stochastic approach of frequency fluctuations [22,33–37]. In this model the energy levels $\varepsilon_{a,b}$ of the system are assumed to fluctuate randomly in time with excursion $\delta\varepsilon_{a,b}(t)$. So, all bath coordinates that are relevant to the dynamics of the two-level system are contained in $\delta\varepsilon_{a,b}(t)$. The basic ensemble-averaged propagator for a density-matrix element $|a\rangle\langle b|$ then has the following form:

$$\langle G_{ab}(t)\rangle = e^{[-i\omega_{ab}-(1/2)\{\gamma_a+\gamma_b\}]t} \times\left\langle\exp\left[-i\int_0^t dt'\delta\omega_{ab}(t')\right]\right\rangle , \quad (8)$$

where $\omega_{ab}=\{\varepsilon_a-\varepsilon_b\}/\hbar$, γ_a and γ_b describe the decay of states $|a\rangle$ and $|b\rangle$, respectively, and $\delta\omega_{ab}(t')=\{\delta\varepsilon_a(t')-\delta\varepsilon_b(t')\}/\hbar$. The population decay processes leading to the rates γ_a and γ_b are assumed to be Markovian here.

When the noise force, denoted by $\delta\omega_{ab}(t')$, is a stationary process with a Gaussian distribution and a zero mean value, the ensemble average of Eq. (8) can be calculated exactly [35,38]. In more general situations, the evaluation of the average can be accomplished by a second-order cumulant expansion [35,39]. The relevant physics of the system-bath coupling is described by the two-time correlation function of the frequency fluctuations, which for a Gauss-Markov process has the following form [40–42]:

$$\langle\delta\omega(t')\delta\omega(t'')\rangle=\Delta^2 e^{-\Lambda|t'-t''|} . \quad (9)$$

Here, Δ is the root-mean-square amplitude of the fluctua-

tions and $\Lambda^{-1}=T_c$ is the correlation time of the interaction between the two-level system and the most important bath degrees of freedom. With this correlation function the averaging of Eq. (8) yields

$$\langle G_{ab}(t)\rangle = e^{[-i\omega_{ab}-(1/2)\{\gamma_a+\gamma_b\}]t} e^{-g(t)} , \tag{10}$$

where the stochastic damping function $g(t)$ has the following form:

$$g(t)=(\Delta^2/\Lambda^2)(e^{-\Lambda t}+\Lambda t-1) . \tag{11}$$

To calculate the nonlinear response of the diagrams of Fig. 3, the factorization of the ensemble-averaged propagator of Eq. (3) into a product of three ensemble-averaged Green's functions of the form of Eq. (10) is not allowed. As discussed above, the reason is of course that the finite correlation time induces a memory in the time evolution of the system [43]. Instead, the ensemble average should be calculated on the product of propagators itself. For diagrams I and II this leads to an identical expression for the stochastic part of the relaxation function, with only population relaxation during time t_2 giving a difference:

$$R^{A}(t_3,t_2,t_1)=e^{-i\omega_{ba}(t_3-t_1)} e^{-(1/2)(\gamma_a+\gamma_b)(t_3+t_1)-(\gamma_{b,a})t_2} \times\left\langle \exp\left[-i\int_{t_1+t_2}^{t_1+t_2+t_3} dt'\delta\omega_{ba}(t')+i\int_0^{t_1} dt'\delta\omega_{ba}(t')\right]\right\rangle . \tag{12a}$$

Here R^{A} refers to part (a) of Fig. 3 (diagrams I and II) and $\gamma_{b,a}$ means γ_b (diagram I) or γ_a (diagram II). Similarly, the relaxation functions for diagrams III and IV also differ only in population relaxation; the stochastic part is identical:

$$R^{B}(t_3,t_2,t_1)=e^{-i\omega_{ba}(t_3+t_1)} e^{-(1/2)(\gamma_a+\gamma_b)(t_3+t_1)-(\gamma_{b,a})t_2} \times\left\langle \exp\left[-i\int_{t_1+t_2}^{t_1+t_2+t_3} dt'\delta\omega_{ba}(t')-i\int_0^{t_1} dt'\delta\omega_{ba}(t')\right]\right\rangle . \tag{12b}$$

The stochastic parts of Eqs. (12a) and (12b) differ only in a $\pm$ sign. This is due to the fact that an inversion of a superposition state occurs in diagrams I and II and not in diagrams III and IV. The finite correlation time between system and bath therefore allows for rephasing of macroscopic coherence in diagrams I and II, while this does not happen in the case of diagrams III and IV. The ensemble averaging of Eqs. (12) can again be performed by using a cumulant expansion [33,37,39]. For Gaussian-Markovian frequency fluctuations [Eq. (9)], the result of this procedure is

$$R_{\mathrm{I}}(t_3,t_2,t_1)=\exp[-i\omega_{ba}(t_3-t_1)-\tfrac{1}{2}(\gamma_a+\gamma_b)(t_3+t_1)-\gamma_b t_2-\Phi^{A}(t_3,t_2,t_1)] , \tag{13a}$$

$$R_{\mathrm{II}}(t_3,t_2,t_1)=\exp[-i\omega_{ba}(t_3-t_1)-\tfrac{1}{2}(\gamma_a+\gamma_b)(t_3+t_1)-\gamma_a t_2-\Phi^{A}(t_3,t_2,t_1)] , \tag{13b}$$

$$R_{\mathrm{III}}(t_3,t_2,t_1)=\exp[-i\omega_{ba}(t_3+t_1)-\tfrac{1}{2}(\gamma_a+\gamma_b)(t_3+t_1)-\gamma_b t_2-\Phi^{B}(t_3,t_2,t_1)] , \tag{13c}$$

$$R_{\mathrm{IV}}(t_3,t_2,t_1)=\exp[-i\omega_{ba}(t_3+t_1)-\tfrac{1}{2}(\gamma_a+\gamma_b)(t_3+t_1)-\gamma_a t_2-\Phi^{B}(t_3,t_2,t_1)] . \tag{13d}$$

Here, the relaxation functions $\Phi^{A,B}(t_3,t_2,t_1)$ can be written in terms of the stochastic damping function $g(t)$ of Eq. (11):

$$\Phi^{A}(t_3,t_2,t_1)=g(t_3)+g(t_1)-[g(t_2)-g(t_3+t_2)-g(t_2+t_1)+g(t_3+t_2+t_1)] =\frac{\Delta^2}{\Lambda^2}[e^{-\Lambda t_3}+e^{-\Lambda t_1}+\Lambda(t_3+t_1)-2+e^{-\Lambda t_2}(e^{-\Lambda t_3}+e^{-\Lambda t_1}-e^{-\Lambda(t_3+t_1)}-1)] , \tag{14a}$$

$$\Phi^{B}(t_3,t_2,t_1)=g(t_3)+g(t_1)+[g(t_2)-g(t_3+t_2)-g(t_2+t_1)+g(t_3+t_2+t_1)] =\frac{\Delta^2}{\Lambda^2}[e^{-\Lambda t_3}+e^{-\Lambda t_1}+\Lambda(t_3+t_1)-2-e^{-\Lambda t_2}(e^{-\Lambda t_3}+e^{-\Lambda t_1}-e^{-\Lambda(t_3+t_1)}-1)] . \tag{14b}$$

A well-known limit of optical dynamics is obtained when the inverse correlation time Λ is much larger than the mean-square amplitude Δ. In that case the dynamics of the system due to the coupling with the bath occurs on times t that are much larger than the correlation time $(\Lambda)^{-1}$. This is the fast modulation limit (or Markovian limit) of optical dynamics. The damping function Eq. (11) can then be approximated by a linear function of time: $g(t)=\Gamma^* t$, where $\Gamma^*\equiv\Delta^2/\Lambda$. This gives exponential relaxation behavior for the basic propagator Eq. (10):

$$\langle G_{ab}(t)\rangle = e^{(-i\omega_{ab}-\Gamma_{ab})t} , \tag{15}$$

where the damping parameter $\Gamma_{ab}=\frac{1}{2}(\gamma_a+\gamma_b)+\Gamma^*$. Taking the inverse of these parameters gives the familiar relation $(T_2)^{-1}=(2T_1)^{-1}+(T_2^*)^{-1}$. Since the correlation time is very short on the time scale of the dynamics, memory effects are now unimportant. The nonlinear response functions R_{I}–R_{IV} can thus be obtained by simply multiplying three ensemble-averaged propagators of the form of Eq. (15), or by taking the proper limit for the

damping functions $g(t)$ in Eqs. (13) and (14). The result is a perturbative form of the optical Bloch equations [44,45]:

$$R_{\rm I}(t_3,t_2,t_1)=\exp[-i\omega_{ba}(t_3-t_1)-\Gamma_{ab}(t_3+t_1)-\gamma_b t_2]\ , \tag{16a}$$

$$R_{\rm II}(t_3,t_2,t_1)=\exp[-i\omega_{ba}(t_3-t_1-\Gamma_{ab}(t_3+t_1)-\gamma_a t_2]\ , \tag{16b}$$

$$R_{\rm III}(t_3,t_2,t_1)=\exp[-i\omega_{ba}(t_3+t_1)-\Gamma_{ab}(t_3+t_1)-\gamma_b t_2]\ , \tag{16c}$$

$$R_{\rm IV}(t_3,t_2,t_1)=\exp[-i\omega_{ba}(t_3+t_1)-\Gamma_{ab}(t_3+t_1)-\gamma_a t_2]\ . \tag{16d}$$

So, in the fast modulation (Markovian, Bloch) limit, the propagation in all diagrams I–IV due to the system-bath coupling is the same; the response functions differ only in population relaxation and a time-dependent phase factor. In the more general stochastic modulation model of Eqs. (13) and (14), diagrams I and II describe different behavior than diagrams III and IV, due to the presence or absence of rephasing processes. In even more general approaches, such as the Brownian oscillator model, the propagation due to the system-bath coupling differs for all four diagrams. This is briefly discussed in the Appendix. Since the most important feature of chirped nonlinear scattering will turn out to be the sensitivity to the time scale(s) of memory in the system propagation, we will use here the simplest approach that can take care of memory effects, i.e., the stochastic model.

III. CHIRPED FOUR-WAVE MIXING

A. General expressions

With the results of the previous chapter it is straightforward to evaluate expressions for four-wave mixing under general excitation conditions, including the use of chirped optical pulses. The central formula is the nonlinear polarization equation (7) with the stochastic relaxation functions given by Eqs. (13). For a linearly chirped pulse, with instantaneous frequency $\omega(t)=\omega^0+bt$, the time-dependent fields $E_j(t)$ have the following form:

$$\begin{aligned}E_j(t)&=a_j(t)\exp\left[-i\int_0^t\omega_j(t')dt'\right]\\&=a_j(t)e^{-i[\omega_j^0+(b_j/2)t]t}\ .\end{aligned} \tag{17}$$

Here $a_j(t)$ is the pulse amplitude envelope, ω_j^0 is some offset frequency, and b_j is the chirp rate. It now suffices to insert Eqs. (13) and (17) in Eq. (7) to obtain the central expression for chirped nonlinear scattering. Thus, the nonlinear polarization that applies to the beam geometry of Fig. 1 and the stochastic model for system frequency fluctuations is

$$\begin{aligned}P(\mathbf{r},t,\tau)=(2i\hbar)^{-3}|\mu_{ab}|^4 e^{i(2\mathbf{k}_2-\mathbf{k}_1)\cdot\mathbf{r}}\int_0^\infty dt_3\int_0^\infty dt_2\int_0^\infty dt_1 e^{-(1/2)(\gamma_a+\gamma_b)(t_3+t_1)}(e^{-\gamma_a t_2}+e^{-\gamma_b t_2})\\ \times\{a_2(t-\tau-t_3)a_2(t-\tau-t_3-t_2)a_1^*(t-t_3-t_2-t_1)\exp[-\Phi^A(t_3,t_2,t_1)-i\Psi^A(t,\tau,t_3,t_2,t_1)]\\ +a_2(t-\tau-t_3)a_1^*(t-t_3-t_2)a_2(t-\tau-t_3-t_2-t_1)\exp[-\Phi^B(t_3,t_2,t_1)-i\Psi^B(t,\tau,t_3,t_2,t_1)]\}\ .\end{aligned} \tag{18}$$

The contributions of diagrams I and II of Fig. 3 are grouped together to give the first part of Eq. (18) with functions Φ^A and Ψ^A, while diagrams III and IV give rise to the second part with functions Φ^B and Ψ^B. The damping functions Φ^A and Φ^B [given by Eqs. (14)] result from the coupling of the system with the bath. The oscillatory parts Ψ^A and Ψ^B contain the system and field frequencies and describe the resonance that occurs when the carrier frequency of the field sweeps through the system transition frequency. Their explicit form is

$$\begin{aligned}\Psi^A(t,\tau,t_3,t_2,t_1)&=\omega_{ba}(t_3-t_1)+\omega_2^0(2t-2\tau-2t_3-t_2)-\omega_1^0(t-t_3-t_2-t_1)\\&\quad+\frac{b_2}{2}[(t-\tau-t_3)^2+(t-\tau-t_3-t_2)^2]-\frac{b_1}{2}(t-t_3-t_2-t_1)^2\ ,\end{aligned} \tag{19a}$$

$$\begin{aligned}\Psi^B(t,\tau,t_3,t_2,t_1)&=\omega_{ba}(t_3+t_1)+\omega_2^0(2t-2\tau-2t_3-t_2-t_1)-\omega_1^0(t-t_3-t_2)\\&\quad+\frac{b_2}{2}[(t-\tau-t_3)^2+(t-\tau-t_3-t_2-t_1)^2]-\frac{b_1}{2}(t-t_3-t_2)^2\ .\end{aligned} \tag{19b}$$

In an experiment such as that of Fig. 1, in which two beams are delayed with respect to each other, the signal itself is usually not time resolved. Instead, the cycle-averaged field energy density is integrated by the detector over all times t, and a signal trace is recorded as a function of delay time τ. The signal that is sampled at a given delay time therefore is proportional to the integral of the polarization of Eq. (18) squared:

$$I_{\rm signal}(\mathbf{r},\tau)\propto\int_0^\infty dt|P(\mathbf{r},t,\tau)|^2\ . \tag{20}$$

Thus, all relevant physics of chirped nonlinear optical interactions is contained in Eqs. (18)–(20). Unfortunately, these equations are not very transparent, and numerical calculations of the integrals will generally be neces-

sary to evaluate the nonlinear response under specific experimental situations. It is useful to discuss first the limits of very fast and very slow chirp rate, since these can be evaluated analytically. The results provide qualitative insight in the chirp-rate dependence of the nonlinear signals, and establish a connection between the physics of Eqs. (18)–(20) and more conventional forms of optical nonlinear interactions.

B. The impulsive limit

In the limit of very fast chirp the envelope of the pulses approaches a δ-function shape. All frequency components of the field are then present within the relevant relaxation times of the system. In such a situation the delayed experiment of Fig. 1 should yield results that resemble those of a conventional photon-echo experiment, in which ultrashort transform-limited pulses are delayed with respect to each other. The limit of very fast chirp can be calculated by applying a well-known analytical form of the δ function [46] to the optical field of Eq. (17):

$$\lim_{b\to\infty} E_j(t)=a_j^0\delta(t) , \tag{21}$$

where a_j^0 is a measure of the pulse area.

When Eq. (21) instead of Eq. (17) is used in Eq. (7), the threefold time integrations of the nonlinear polarization are readily performed. The nonlinear polarization that applies to very fast chirp rates then is

$$P(\mathbf{r},t,\tau)=(2i\hbar)^{-3}|\mu_{ab}|^4 e^{i(2\mathbf{k}_2-\mathbf{k}_1)\cdot\mathbf{r}}(a_2^0)^2(a_1^0)^* e^{-i\omega_{ba}(t-2\tau)} e^{-(1/2)(\gamma_a+\gamma_b)t}$$
$$\times[2e^{-\Phi^A(t-\tau,0,\tau)}H(t-\tau)H(0)H(\tau)+(e^{\gamma_a\tau}+e^{\gamma_b\tau})e^{-\Phi^B(t-\tau,\tau,-\tau)}H(t-\tau)H(\tau)H(-\tau)] . \tag{22}$$

The Heaviside functions $H(t)$ result from the integrations over the δ functions with delay times t_1, t_2, and t_3 defined to be positive. The first term of Eq. (22) contains the contributions from diagrams I and II of Fig. 3 to the polarization. The Heaviside functions of this part stipulate that $\tau\geq 0$ and $t\geq\tau$, so the signal in the direction $2\mathbf{k}_2-\mathbf{k}_1$ is induced only when beam $\mathbf{k}_2$ interacts after beam $\mathbf{k}_1$, and the signal appears only after both pulses have interacted with the sample. The second part of Eq. (22) results from diagrams III and IV. It follows that there is no contribution from these terms to the signal at any delay, except for a δ-function contribution at $\tau=0$.

In the impulsive limit, at very high chirp rates, the nonlinear response is completely determined by the quantum-mechanical pathways I and II depicted in Fig. 3.

The function $\Phi^A(t-\tau,0,\tau)$ that describes the non-Markovian, stochastic damping of the signal due to system-bath interactions, follows from Eq. (14a):

$$\Phi^A(t-\tau,0,\tau)=\frac{\Delta^2}{\Lambda^2}[2e^{-\Lambda(t-\tau)}+2e^{-\Lambda\tau}-e^{-\Lambda t}+\Lambda t-3] . \tag{23}$$

This expression is well known and was published in many forms in connection with two-pulse photon-echo generation in the impulsive limit [22,27,39,47–49]. The signal is called a photon echo because rephasing of a macroscopic coherence causes the signal to peak at a certain delay relative to the interaction with the second beam. This is possible due to the inversion of a superposition state in diagrams I and II, and the memory which results from the non-Markovian character of propagation. In the stochastic model the influence of memory is restricted to times that are within the correlation time $(\Lambda)^{-1}$ of the system-bath interaction.

C. The steady-state limit

In the limit of very slow chirp, the instantaneous frequency of the pulses does not change within the relevant relaxation times of the system. The integrations of the nonlinear polarization Eq. (7) may then be performed as if the frequencies and the amplitudes of both beams do not change at all. This means that for every time t we can assume that Eq. (17) can be replaced by

$$E_j(t)\approx a_j^c e^{-i\omega_j^c t} , \tag{24}$$

where a_j^c and ω_j^c are constant. In this limit the experiment of Fig. 1 resembles a frequency domain experiment with steady-state fields.

When Eq. (24) instead of Eq. (17) is used in Eq. (7), the nonlinear polarization that applies to very slow chirp rates can be written as

$$P(\mathbf{r},t,\tau)=(2i\hbar)^{-3}|\mu_{ab}|^4 e^{i(2\mathbf{k}_2-\mathbf{k}_1)\cdot\mathbf{r}}(a_2^c)^2(a_1^c)^* e^{-i(2\omega_2^c-\omega_1^c)t+2i\omega_2^c\tau}$$
$$\times[\Omega_{\mathrm{I}}(s_3,s_2^b,s_1^+)+\Omega_{\mathrm{II}}(s_3,s_2^a,s_1^+)+\Omega_{\mathrm{III}}(s_3,s_2^b,s_1^-)+\Omega_{\mathrm{IV}}(s_3,s_2^a,s_1^-)] . \tag{25}$$

Here the four functions $\Omega_{\mathrm{I-IV}}$ apply to the four diagrams I–IV of Fig. 3, respectively. They are Fourier-Laplace transforms that are defined as

$$\Omega_{\mathrm{I,II}}(s_3,s_2^{b,a},s_1^{+})=\int_0^{\infty}dt_3\int_0^{\infty}dt_2\int_0^{\infty}dt_1 e^{-s_3t_3}e^{-s_2^{b,a}t_2}e^{-s_1^{+}t_1}e^{-\Phi^{A}(t_3,t_2,t_1)}, \tag{26a}$$

$$\Omega_{\mathrm{III,IV}}(s_3,s_2^{b,a},s_1^{-})=\int_0^{\infty}dt_3\int_0^{\infty}dt_2\int_0^{\infty}dt_1 e^{-s_3t_3}e^{-s_2^{b,a}t_2}e^{-s_1^{-}t_1}e^{-\Phi^{B}(t_3,t_2,t_1)}, \tag{26b}$$

with the functions $\Phi^{A,B}(t_3,t_2,t_1)$ given by Eqs. (14) and the frequency domain variable s defined by

$$s_3=-i(2\omega_2^c-\omega_1^c-\omega_{ba})+\tfrac{1}{2}(\gamma_a+\gamma_b), \tag{27a}$$

$$s_2^{a,b}=-i(\omega_2^c-\omega_1^c)+\gamma_{a,b}, \tag{27b}$$

$$s_1^{+}=+i(\omega_1^c-\omega_{ba})+\tfrac{1}{2}(\gamma_a+\gamma_b), \tag{27c}$$

$$s_1^{-}=-i(\omega_2^c-\omega_{ba})+\tfrac{1}{2}(\gamma_a+\gamma_b). \tag{27d}$$

These Fourier-Laplace transforms of the stochastic relaxation functions can be calculated as expansions of continued fractions [35,50,51]. The expressions for diagrams I and II can be denoted as

$$\Omega_{\mathrm{I,II}}(s_3,s_2^{b,a},s_1^{+})=\sum_{n=0}^{\infty}\frac{\Delta^{2n}}{n!\Lambda^{2n}}J_n(s_3)\frac{1}{s_2^{b,a}+n\Lambda}J_n(s_1^{+}). \tag{28}$$

For diagrams III and IV the expression is identical except for an additional multiplication factor of $(-1)^n$ and a replacement of s_1^{+} by s_1^{-}. The functions J_n are generated by the recursion relation [50]:

$$\frac{\Delta^2}{\Lambda}J_1(s)=1-sJ_0(s), \tag{29a}$$

$$\frac{\Delta^2}{\Lambda}J_{n+1}(s)=n\Lambda J_{n-1}(s)-(s+n\Lambda)J_n(s). \tag{29b}$$

This gives for the first term J_0:

$$J_0(s)=\cfrac{1}{s+\cfrac{\Delta^2}{s+\Lambda+\cfrac{2\Delta^2}{s+2\Lambda+\cfrac{3\Delta^2}{s+3\Lambda+\cdots}}}}. \tag{30}$$

This rather complicated result for the frequency domain nonlinear response function in the stochastic model is not very well known. In the Markovian (Bloch) limit the expressions simplify considerably. As discussed in Sec. II, this limit is reached when the inverse correlation time Λ is much larger than the root-mean-square amplitude Δ of the fluctuations. It follows that $(\Delta/\Lambda)^2\ll 1$, and hence all terms with $n>0$ can be neglected in Eq. (28). The transforms in the Bloch limit can thus be written as

$$\Omega_{\mathrm{I,II}}(s_3,s_2^{b,a},s_1^{+})=J_0(s_3)\frac{1}{s_2^{b,a}}J_0(s_1^{+}), \tag{31a}$$

$$\Omega_{\mathrm{III,IV}}(s_3,s_2^{b,a},s_1^{-})=J_0(s_3)\frac{1}{s_2^{b,a}}J_0(s_1^{-}). \tag{31b}$$

In the Markovian limit it also follows that $J_0(s)\simeq(s+\Gamma^*)^{-1}$ with $\Gamma^*=\Delta^2/\Lambda$ (see Sec. II). Using this form, the frequency domain nonlinear response functions can be written as a product of Lorentzian line shapes:

$$\Omega^{\mathrm{I,II}}(s_3,s_2^{b,a},s_1^{+})=[-i(2\omega_2^c-\omega_1^c-\omega_{ba})+\tfrac{1}{2}(\gamma_a+\gamma_b)+\Gamma^*]^{-1}\times[-i(\omega_2^c-\omega_1^c)+\gamma_{a,b}]^{-1}[+i(\omega_1^c-\omega_{ba})+\tfrac{1}{2}(\gamma_a+\gamma_b)+\Gamma^*]^{-1}, \tag{32a}$$

$$\Omega^{\mathrm{III,IV}}(s_3,s_2^{b,a},s_1^{-})=[-i(2\omega_2^c-\omega_1^c-\omega_{ba})+\tfrac{1}{2}(\gamma_a+\gamma_b)+\Gamma^*]^{-1}\times[-i(\omega_2^c-\omega_1^c)+\gamma_{a,b}]^{-1}[-i(\omega_2^c-\omega_{ba})+\tfrac{1}{2}(\gamma_a+\gamma_b)+\Gamma^*]^{-1}. \tag{32b}$$

When all functions $\Omega_{\mathrm{I-IV}}$ are added to calculate the full response, the result of Eqs. (32) is identical to the one that was derived before by Yajima and Souma [52].

The most important result for the purpose of this paper is that in the slow chirp limit all quantum-mechanical pathways I–IV of Fig. 3 contribute to the nonlinear polarization equation (25). In general, the relative magnitudes of these contributions will depend on the values for the relaxation parameters. This will be discussed more extensively in Sec. IV where numerical calculations are presented. In some circumstances all pathways contribute equally, for other values of the dynamic parameters one or several diagrams dominates the nonlinear response. In principle, however, all diagrams have to be taken into account.

In the steady-state limit, at very low chirp rates, the nonlinear response is determined by all quantum-mechanical pathways (I–IV of Fig. 3) that are relevant to the experimental configuration.

D. Synopsis

The following is what makes chirped nonlinear scattering special for studies of optical dynamics: when the chirp rate is such that the optical frequency sweeps through a material resonance fast compared to the sys-

tem dynamics, two quantum-mechanical pathways (I and II of Fig. 3) determine the signals that are generated. When the chirp rate is adjusted such that the field sweeps through the resonance slow compared to the system dynamics, these two pathways still contribute with somewhat changed values for the interaction parameters. The crucial point, however, is that now two new quantum-mechanical pathways (III and IV of Fig. 3) contribute as well, which gives rise to interferences with the original diagrams.

Since the character of both kinds of diagrams is completely different, the nonlinear optical signals that are generated are a clear signature of the limit in which the polarization is induced. Experimentally, the chirp rate can be adjusted over orders of magnitude, so the technique can be exploited to study dynamics over a very large time range. It is impossible to give analytical expressions for the transition from fast to slow chirp, so the details of this change will have to be evaluated numerically.

IV. CALCULATIONS

A. The integration procedure

When the chirp rate of the optical fields is not much faster or slower than the relevant system dynamics, Eqs. (18)–(20) have to be used without simplification to describe the nonlinear experiments. This means that a four-dimensional time integral has to be evaluated. The results thus obtained are exact within the limits of the perturbative approach and the rotating wave approximation (Sec. II). As an example, chirped four-wave mixing will be analyzed with the room-temperature dynamical parameters of resorufin dissolved in dimethylsulfoxide (see Fig. 2). These parameters are known from a previous study in which ultrashort, transform-limited pulses were used [22]. For the stochastic model it was found that the inverse correlation time between system and bath is $\Lambda=27$ THz ($T_c=37$ fs) and the root-mean-square amplitude of the fluctuation is $\Delta=41$ THz (except for Λ all numbers cited in the text are angular frequencies). The width of the (linear) absorption line shape, which is given by the Fourier-Laplace transform of Eq. (10), is 50 THz half width at half maximum (HWHM). Population relaxation can be neglected on the time scale of the system-bath dynamics and the time scale of relevant experiments.

The calculation of the chirped nonlinear polarization and the resulting signal was performed using two separate integration routines. The threefold integrals of Eq. (18) are best handled by Monte Carlo integration, since the nonlinear response function oscillates rapidly according to the functions $\Psi^{A,B}(t,\tau,t_3,t_2,t_1)$ of Eqs. (19). The advantage of this type of numerical integration is that it can handle wild functions in many dimensions very efficiently [53,54]. The real and imaginary parts of Eq. (18) were calculated separately using an adaptive multidimensional Monte Carlo integration routine from the NAG library [55]. The precision was set at an estimated 2% of the total value. In order to reduce the calculation time as much as possible, the upper boundaries of these integrals had to be chosen carefully. Subsequently, the integral over time of Eq. (20) was performed by the Romberg integration method [54], in which a function is sampled at equidistant points and the sampling density is increased until (after extrapolation) the chosen precision (2.5%) is met. The integration range considered in this procedure was limited to times where

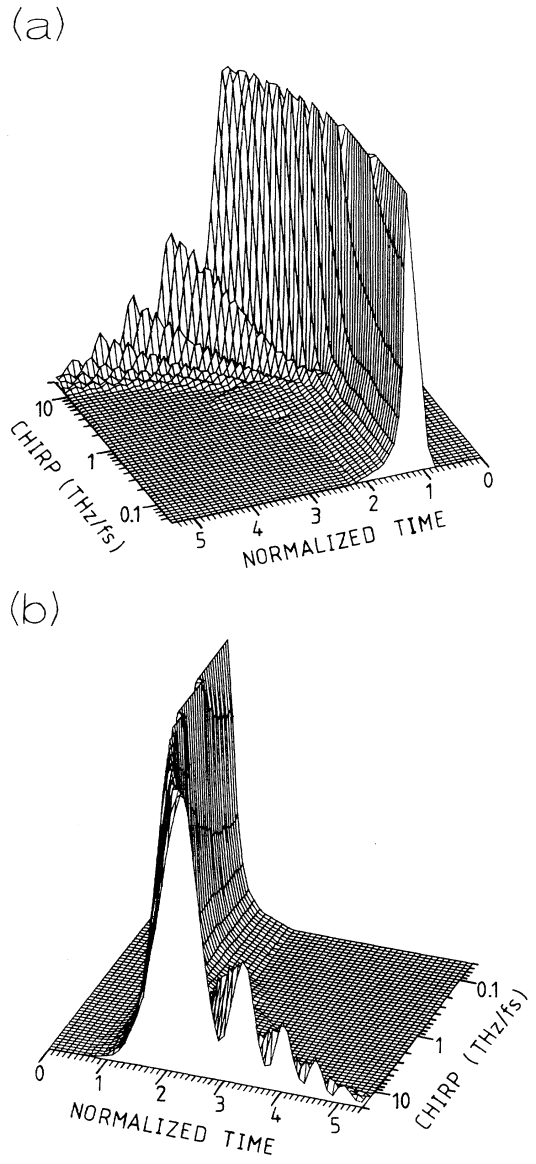

FIG. 4. Nonlinear cycle-averaged polarization as a function of normalized time for different chirp rates of the inducing fields. At time 1.0 the instantaneous frequency of beam $\mathbf{k}_1$ is at the maximum of the frequency response of the system. The delay between beams $\mathbf{k}_1$ and $\mathbf{k}_2$ is taken to be $\tau=0$ fs; the maximum of the polarization is normalized. (a) and (b) are the same plots viewed from two different angles. The system dynamics was modeled by a stochastic modulation of the transition frequency with parameters $\Lambda=27$ THz and $\Delta=41$ THz. When positive delay $\tau>0$ is introduced, the polarization maximum for very fast chirp rates shifts to larger normalized times.

$|P(\mathbf{r},t,\tau)|^2$ was at least 2% of the maximum value. The most extensive calculations, such as those required to construct the two-dimensional polarizations of Fig. 4, took about 16 h cpu time on a Convex C240 minisupercomputer.

Beams $\mathbf{k}_1$ and $\mathbf{k}_2$ of Fig. 1 usually derive from the same laser by means of beam splitters in the optical setup. Experimentally, it is quite feasible to manipulate the phases of the beams separately, giving rise to different chirp rates in both beams. This may lead to, for instance, nonlinear signals that are compressed in time compared to the original chirped pulses [56]. We will not consider this situation here, and limit ourselves to the case where the chirp rates of beams $\mathbf{k}_1$ and $\mathbf{k}_2$ are identical: $b_1=b_2\equiv b$. Also, we will take the frequency spectrum of the light fields to be much wider than the width of the optical resonance(s) of the system. This means that for the numerical evaluation the exact value of the offset frequency $\omega_1^0=\omega_2^0\equiv\omega^0$ is not very important. It may be the lowest frequency that the pulses carry, but any frequency away from the material resonances will do. In addition, when the spectral distribution of the pulses is reasonably flat, we can take the amplitudes of the fields to be constant: $a_{1,2}(t)\equiv a_{1,2}^0$. The rise and fall of the pulse amplitude when the instantaneous optical frequency is well outside the material resonances are of no consequence to the nonlinear response.

B. The nonlinear polarization

In Fig. 4 the absolute square of the third-order nonlinear polarization equation (18) is shown as a function of the chirp rate of the pulses. The time axis is normalized such that the instantaneous frequency sweeps in unit time from its starting value outside of the system resonance to the frequency of the absorption maximum. In the calculation the lowest frequency of the positively chirped pulse was taken to be $\omega^0=2900$ THz (650 nm) while the resonance frequency was at $\omega_{ba}=3165$ THz (596 nm). This is the absorption maximum of the pure electronic transition of resorufin dissolved in dimethylsulfoxide. For the slowest chirp rate shown ($b=0.05$ THz/fs), the instantaneous frequency sweeps in real time from its offset value to the system transition frequency in 5.3 ps; for the fastest chirp rate ($b=20$ THz/fs) this occurs in 13.3 fs.

The excitation conditions of Fig. 4 range from the steady state to the impulsive limit. On the slow chirp side, the field frequency sweeps through the material resonance in a time that is long compared to the system dynamics. The cycle-averaged nonlinear polarization then has a smooth profile and peaks at unity of normalized time, i.e., when the instantaneous optical frequency is equal to the absorption maximum. When the chirp rate is increased, the material response cannot follow the instantaneous frequency of the field anymore. As a result, the nonlinear polarization lags behind and shows a maximum in time only when the field frequency is already past the absorption maximum. In addition, pronounced oscillations begin to occur. At the fastest chirp rates shown the field frequency sweeps through the resonance very rapidly compared to the material dynamics. Consequently, the polarization induced at a certain time will continue to precess while the optical fields change their frequency. This leads to destructive or constructive interferences between contributions to the polarization that are induced at different times.

It should be mentioned that somewhat different oscillations have been described for chirped excitation conditions before. These occur in the transmitted intensity of a chirped beam when a linear polarization is induced in a material with a very-narrow-band material resonance [57,58]. The oscillations are caused by the interference between the free induction decay of the material and the inducing chirped field. This feature can be employed to fully characterize the phases of the chirped pulses at all times [57,58]. In the nonlinear case discussed here the situation is a completely different one: the oscillations occur in the nonlinear polarization itself due to interfering contributions that are induced at different times by phase-shifted optical fields.

When a relative delay is introduced between beams $\mathbf{k}_1$ and $\mathbf{k}_2$, the general picture for the nonlinear polarization remains the same. For slow chirp rates the traces are indistinguishable from those at zero delay. Since the instantaneous frequency of both beams is not the same anymore, the overall amplitude of the polarization will be different. This aspect will be treated below. For fast chirp rates the polarization is delayed even more compared to the time at which the instantaneous optical frequency is at the maximum of the material resonance. This is due to the fact that rephasing processes begin to dominate the nonlinear response (Sec. III). The nonlinear polarization then becomes "photon-echo-like" and hence experiences an extra delay with respect to the times at which interactions between system and fields occur. For delays large compared to the ratio of system dynamics to chirp rate, the pulses sweep through the resonance one after the other, and a true photon echo is induced.

C. Delayed nonlinear signals

Shown in Fig. 5 is how, for a few optical chirp rates, the signal varies as a function of relative pulse delay τ. The signal is the polarization equation (18) squared and integrated over time t [Eq. (20)]. When the optical field sweeps through the system resonance in a time long compared to the system dynamics, the signal is fairly symmetric around delay time $\tau=0$ fs (dotted and dashed curves). For a chirp rate $b=1.35$ THz/fs, the fields sweep through the 50-THz-wide resonance (HWHM) of the system in a time that is equal to the correlation time $T_c=\Lambda^{-1}=37$ fs of the system-bath dynamics. It is clear from Fig. 5 that for larger values of b the signal maximum shifts away from zero and now occurs at a finite delay (dot-dashed curve).

For even faster chirp rates (solid curve), the signal trace becomes very asymmetric around the maximum value, with the gentler slope extending for positive delays (beam $\mathbf{k}_2$ after $\mathbf{k}_1$). This is reminiscent of standard photon-echo experiments on systems with memory in the dynamics, such as inhomogeneous broadening or a finite correlation time between the system and the bath (Sec.

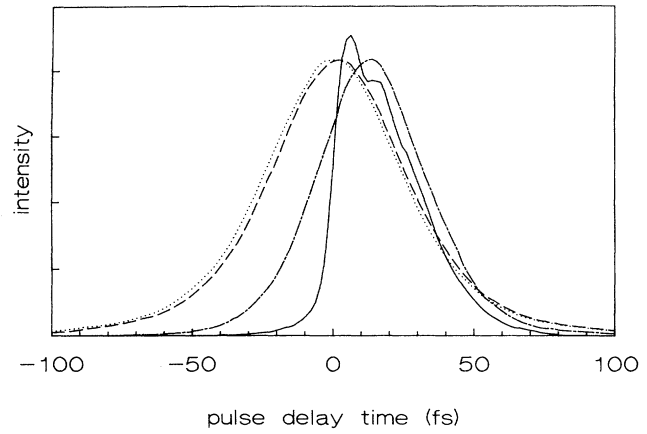

FIG. 5. Delay dependence of the time-integrated signal intensity for four different chirp rates of the optical fields. The chirp rates b are 0.02 THz/fs (dotted curve), 0.2 THz/fs (dashed curve), 2 THz/fs (dot-dashed curve), and 20 THz/fs (solid curve). The system dynamics is as in Fig. 4.

II). Rephasing processes apparently begin to dominate the signal. In fact, the signal calculated for such fast chirped excitation can be directly compared to the analytical result that is known for δ pulse excitation. This was treated in Sec. III. In the stochastic model the nonlinear polarization for excitation of infinitely short duration is given by the first term of Eq. (22), with a damping function given by Eq. (23). The signal is the usual integral over the polarization squared [Eq. (20)].

The comparison between the numerical evaluation for optical fields with a chirp rate $b=20$ THz/fs and the analytical result for δ pulse excitation is shown in Fig. 6. From the resemblance between both curves it can be concluded that in this limit chirped excitation indeed occurs impulsively. The asymmetric behavior is apparently caused by a photon-echo type of emission. The major

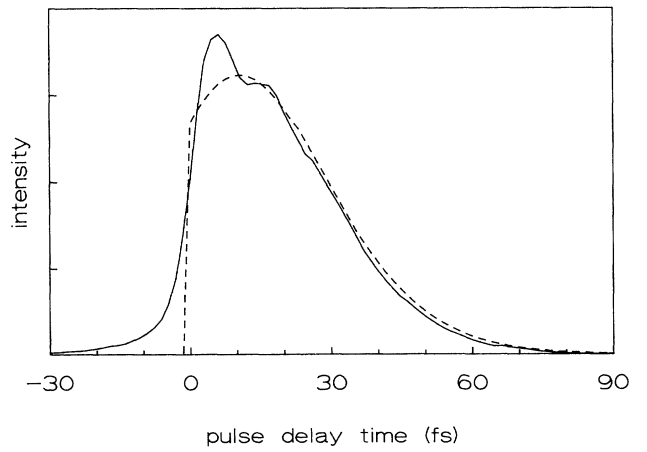

FIG. 6. Nonlinear signal expected for δ-shaped optical pulses (dashed line) and for chirped excitation (solid line). The chirp rate is fast compared to the system dynamics: $b=20$ THz/fs. The system dynamics is as in Fig. 4.

difference between both traces is of course the structure that is present for delays $\tau \leq 10$ fs in the chirped excitation case. Both this structure and the finite positive slope of the chirped trace are due to the fact that a fast chirp is not yet an infinite chirp.

In diagrams III and IV of Fig. 3 the time ordering of the light fields is E_2, then E_1, then E_2 again. When two δ-shaped pulses are applied, it is impossible to realize this time ordering at finite delays, and only diagrams I and II are of importance then. For infinitely fast chirped pulses the situation is the same: diagrams I and II dominate the signal. This is discussed in Sec. III. Diagrams III and IV of Fig. 3 in principle only contribute when the required time ordering of the field interactions can be accomplished, i.e., in circumstances where the interactions between system and fields hold on for a certain duration. For instance, in time-resolved experiments with transform-limited fields they only contribute when pulses of finite duration overlap in time and then they give rise to features that may be called coherent artifacts.

For chirped pulses a similar behavior is expected: when the chirp rate is fast compared to the system dynamics and the excitation occurs impulsively the importance of these diagrams for the overall signal is small, but remains significant at (or near) delay time $\tau=0$ fs. This causes the bump at small delay in the solid trace of Fig. 6. When the signal is calculated for even faster chirp rates, the peak that is due to diagrams III and IV becomes narrower and moves further to delay $\tau=0$. Finally, for infinitely fast chirp rates the δ-function contribution is obtained that was calculated analytically as the second term of Eq. (22).

The behavior of the various diagrams of Fig. 3 in chirped pulse scattering can be elucidated further if we look at their relative importance when the chirp rates are slower. In Fig. 7 the calculated signal is shown for a

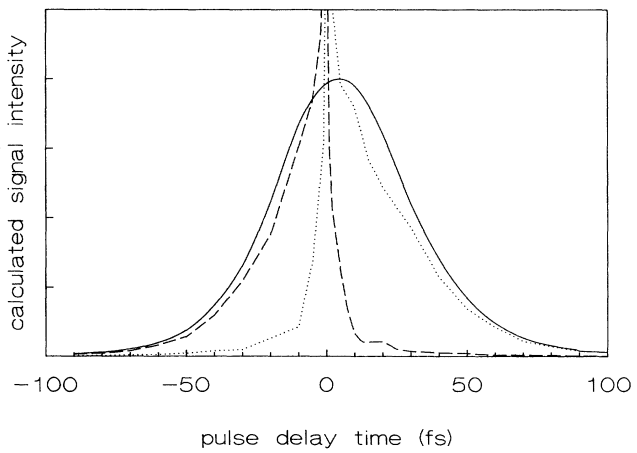

FIG. 7. Nonlinear chirped signal for pulses with a chirp rate $b=0.5$ THz/fs (solid line). When only diagrams I and II of Fig. 3 are used in the calculation, the dotted line results. Diagrams III and IV of Fig. 3 lead to a signal trace given by the dashed line. The infinities at delay $\tau=0$ fs cancel when the contributions from all diagrams are included in the calculation. The system dynamics is as in Fig. 4.

chirp rate of $b=0.5$ THz/fs. This is the same chirp rate that was used in the nonlinear experiment on solvated resorufin that is depicted in Fig. 2. The dotted and dashed curves are the amplitudes squared of diagrams I and II, and of diagrams III and IV, respectively. The shapes of these curves are typical for the dynamical response of the material when propagated according to both kinds of quantum-mechanical pathways. Even for this relatively low chirp rate (it takes the fields 100 fs to sweep across the HWHM line breadth), the contribution from diagrams I and II is distinctly asymmetric. The tail that stretches out on the positive delay side is somewhat longer than for fast chirped excitation (see Fig. 6). Due to the relatively slow chirp, diagrams III and IV now contribute for finite delays as well. Since this occurs mainly on the negative delay side of the trace, they tend to symmetrize the signal. As discussed above, for chirp rates fast compared to the system dynamics their contribution becomes strongly peaked around delay time $\tau=0$ fs and the asymmetric curve of Fig. 6 is obtained. The presence or absence of asymmetry with a certain chirp rate of the fields therefore is a clear indication of the time scale(s) on which system dynamics takes place.

Around $\tau=0$ fs the integrals of Eq. (18) for the nonlinear polarization diverge if the contributions from both kinds of diagrams are calculated separately. As can be seen in Fig. 7 their respective amplitudes interfere in such a way that these integrals do converge when the nonlinear polarization is calculated properly, taking all amplitudes of all pathways into account. The fact that the divergences are removed when all terms are calculated is very fundamental [59]. When the time ordering of interactions with different fields is changed, there *has* to be a point where all diagrams must be taken into account. This is also the significance of the δ-function contribution in the second part of Eq. (22) which was calculated for δ pulse excitation.

D. Experiment versus calculation

The calculated curve for delayed nonlinear chirped scattering in a two-level system with non-Markovian stochastic frequency fluctuations is compared in Fig. 8 with the experimental result on resorufin in dimethylsulfoxide. Considering that no fitting was involved at all, the agreement between both curves is excellent. As discussed above, the rather symmetric shape indicates that diagrams III and IV of Fig. 3 contribute substantially, and hence it can be concluded that the chirp rate is relatively slow compared to the system dynamics. Apparently there is not much memory in the electronic two-level system of resorufin on a time scale of 100 fs (i.e., the time it takes the field to sweep across the system resonance).

In more sophisticated dynamical models, such as those based on Brownian oscillators, the result of the calculation is almost identical to that of the stochastic model. This is also shown in Fig. 8. Such models also incorporate next to femtosecond fluctuations an ultrafast shift of the system energy levels. These occur in liquids due to the rearrangement of the bath upon excitation of the system [60–63]. The physics of Brownian oscillators is briefly discussed in the Appendix. For an overdamped

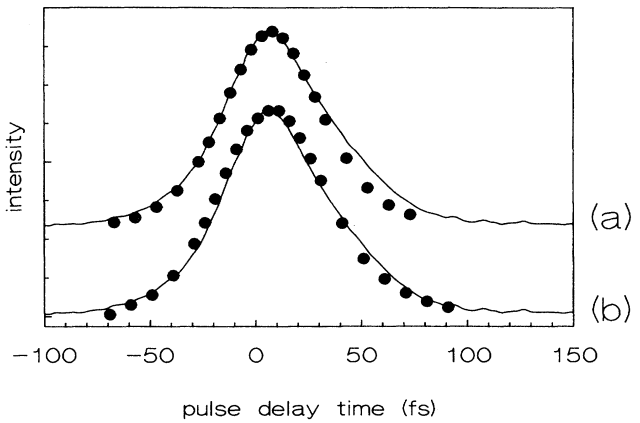

FIG. 8. Comparison of calculated nonlinear delayed signals (dots) with the experimental result on resorufin dissolved in dimethylsulfoxide (solid traces). The experimental traces are identical to the chirped pulse result of Fig. 2. In the upper part (a) the system dynamics is modeled by stochastic fluctuations of the transition frequency with the parameter values $\Lambda=27$ THz and $\Delta=41$ THz. In the lower trace (b) an overdamped Brownian oscillator is used to simulate the dynamics. The variance of displacement Δ and the correlation time Λ^{-1} where taken to be identical to those of the stochastic model; in addition, a rapid shift of the energy levels is incorporated which occurs on a time scale of $(\Lambda)^{-1}$ over a range of $\hbar\Delta^2/2kT=23$ THz.

Markovian Brownian oscillator the energy shifts are directly related to the fluctuations, and in the calculations for Fig. 8 again no fitting was involved at all. Although the agreement with the experiment seems to be somewhat better in the trailing part of the delayed signal trace, the improvement is hardly significant. Apparently, the experiment is in this case not very sensitive to details in the interaction between system and bath; the time scale of the dynamics compared to the chirp rate governs the experiment and determines the shape of the generated signals.

Suppose now that there exists a separation of time scales in the system dynamics. This is a common situation in solid- and gas-phase systems, where often some kind of inhomogeneous broadening is present. In such a case, the nonlinear polarization equation (18) has to be labeled by the transition frequency ω_{ba}, and a summation has to be performed over the distribution $g(\omega_{ba})$ of transition frequencies that is present during a relevant time span:

$$P^{(3)}_{\text{inhomogeneous}}(\mathbf{r},t,\tau) = \int_{-\infty}^{\infty} d\omega_{ba} P(\omega_{ba},\mathbf{r},t,\tau) g(\omega_{ba}) \,. \quad (33)$$

If the inhomogeneous width is substantial, it readily follows that only the first part of Eq. (18) (diagrams I and II) contributes to the nonlinear signal [64]. The argument is the same as before: when the chirp rate is fast compared to the system dynamics (which in this case gives rise to inhomogeneous broadening), the influence of diagrams III and IV is negligible for finite delay times τ due to their lack of rephasing capability. Diagrams I and

II dominate the signal then, and give rise to the typical asymmetric decay traces such as depicted in Fig. 7, with the infinity at $\tau=0$ fs removed by diagrams III and IV. This was experimentally observed in a low-temperature, inhomogeneously broadened solid by Tokizaki, Ishida, and Yajima [18]. Since this asymmetry is not observed here, it can be concluded that there is no inhomogeneous broadening in the system at the time scale that is relevant to the experiment (100 fs). This contradicts with usual assumptions in treatments of optical dynamics in liquid-phase systems [21,25,65–68].

V. CHIRPED COHERENT RAMAN SCATTERING

A. Three-level systems

In real molecules chirped four-wave mixing produces not only signals related to electronic transitions, but also to the vibrational level structure. A dye molecule like resorufin, which consists of 22 atoms, has 60 vibrational modes. However, due to the symmetry of the molecule most of the vibronic transitions carry negligible oscillator strength. We have shown that the absorption spectrum of resorufin can be adequately described by ca. 10 optical transitions [22]. For nonlinear response even fewer modes need to be considered. The four-wave-mixing polarization equation (7) is fourth order in the transition dipole moment, so in general only the strongest transitions contribute significantly to a nonlinear signal. In the case of resorufin only one vibration has to be taken into account [22]. The associated vibrational energy is about 100 THz (radians per second) in both the electronic ground and excited states. The most simple level scheme for nonlinear optical experiments on resorufin therefore consists of four levels. However, we will first discuss chirped four-wave mixing in a three-level system, since the most salient features appear there as well, and are simpler to describe.

Figure 9 shows what kind of situations are possible for chirped four-wave mixing in a three-level system. At small delays [Fig. 9(a)], both beams interact with the same transition at the same time. Hence, for chirp rates small compared to the energy difference between the transitions, the field frequencies sweep through the optical resonances one at a time. The nonlinear signals that are generated by the two successive two-level interactions arrive at the detector independently and add up to yield a total signal intensity. In this limit of chirp rate the treatment of previous sections (e.g., Figs. 4–8) remains valid, only the overall intensity is influenced by the presence of the additional system resonance.

When the chirp rate is fast compared to the energy difference between the two optical transitions, both will be excited simultaneously. This leads to the formation of a vibrational wave packet, which in turn gives rise to beats in the decay profiles. These interferences in the nonlinear polarization are well known from impulsive nonlinear scattering experiments [21,22] and will also occur when chirped pulses are used with chirp rates that are fast compared to the inverse frequency difference of the two transitions.

A completely new situation, compared to the two-level results, is encountered when the delay is increased to large values. The instantaneous frequency difference then increases to large values as well (see Fig. 1) and resonances occur on difference frequencies of the optical transitions. Depicted in Fig. 9(b) is how in that case both beams interact with different system transitions at the same time. Thus, the nonlinear signal in the direction $2\mathbf{k}_2-\mathbf{k}_1$ should be classified as chirped coherent Raman scattering. When the delay is positive the instantaneous frequency of $\mathbf{k}_2$ is smaller than that of $\mathbf{k}_1$ so the signal at $2\mathbf{k}_2-\mathbf{k}_1$, enhanced by the multiple resonances, can be classified as coherent Stokes Raman scattering (CSRS). With negative delays the corresponding chirped coherent anti-Stokes Raman signal (CARS) should be generated.

The experimental result that was obtained for resorufin dissolved in dimethylsulfoxide is shown in Fig. 10. The

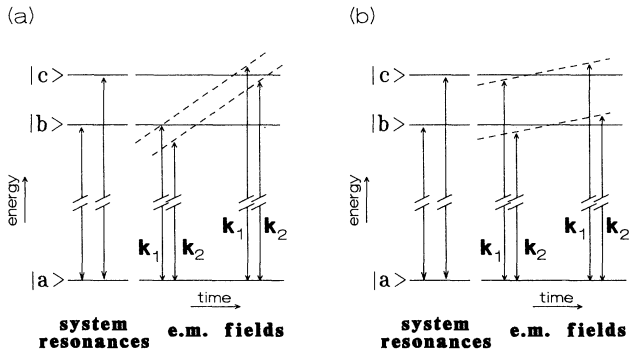

FIG. 9. Chirped optical fields in a three-level system. (a) The instantaneous frequency difference between beams $\mathbf{k}_1$ and $\mathbf{k}_2$ is small compared to the difference frequency of the system. Both beams interact with the same transition at the same time. (b) The delay between both beams is so large that the instantaneous frequencies sweep through two different system resonances at the same time. When, as depicted, $\omega_2(t)<\omega_1(t)$ the nonlinear signal in the direction $2\mathbf{k}_2$-$\mathbf{k}_1$ is chirped-resonance-enhanced coherent Stokes Raman scattering (CSRS).

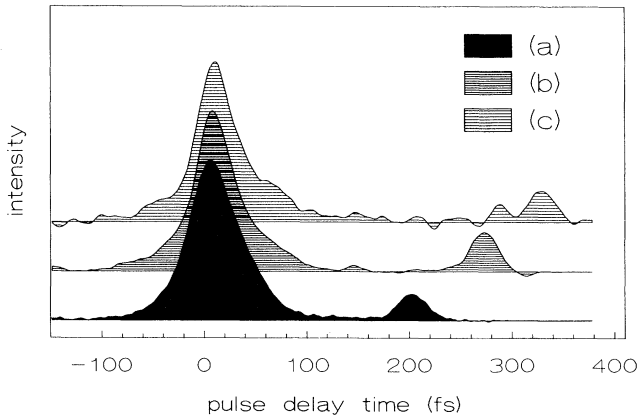

FIG. 10. Two-pulse delayed scattering signal at room temperature for the dye molecule resorufin dissolved in dimethylsulfoxide. The results are shown for three different chirp rates of the pulses: (a) $b=0.5$ THz/fs, (b) $b=0.39$ THz/fs, and (c) $b=0.31$ THz/fs. The Raman features at delays $\tau>200$ fs shift linearly with the chirp rate.

trace obtained with a chirp rate of $b=0.5$. THz/fs is identical to that of Fig. 2, only the window on the range of delay times is increased now. The feature at $\tau=200$ fs indicates a system resonance at $b\tau=100$ THz, which agrees well with the difference between the vibronic transition and the pure electronic transition of resorufin [22]. When the chirp rate is decreased, the delay at which this resonance occurs should increase. Also depicted in Fig. 10 is how the chirped Raman feature indeed shifts with the chirp rate, while the shape of the signal at small delays does not change much at all. This last observation is in accordance with the theory of the previous section. The chirp rate was changed experimentally by placing quartz blocks of various thicknesses in the laser beams to increase the dispersion, and by that the pulse length in the nonlinear experiment. The chirped CARS signal which in principle should be generated at negative delays is not visible, so apparently the amplitude is much less than that of the corresponding CSRS signal.

The Feynman diagrams and system resonances for three-level coherent Raman scattering are depicted in Fig. 11. Excited-state resonances in four-wave mixing were studied extensively in connection with dephasing processes. For steady-state excitation, the resonance on the difference frequency only occurs when dephasing destroys the destructive quantum interference between diagrams I and III. The resonances therefore were called "pressure-induced extra resonance" (PIER-4) in gas-phase experiments [69], and "dephasing-induced coherent emission" (DICE) in condensed-matter four-wave mixing [70,71]. It is also known that in the impulsive limit the resonance at the difference frequency occurs even in the absence of optical dephasing [33,72]. Therefore, with chirped excitation the destructive interference between these two quantum-mechanical pathways will depend on the chirp rate compared to the system dynamics, since this determines to what extent the excitation occurs impulsively. The various resonances at the electronic transitions of the system will be present in any case, so multiple enhancements of the chirped coherent Raman signals will always occur. All these effects, including possible dephasing induced ones, are incorporated in the nonlinear formalism of Sec. II.

The shape of the Raman-type resonances in chirped experiments will in principle be determined by both vibrational and electronic dephasing parameters of the system. However, vibrational dynamics in liquids generally is much slower than electronic dynamics. This can, for instance, be deduced from the fact that optical spectra in liquids generally are rather broad and structureless compared to Raman spectra of the same substance. When we neglect vibrational damping altogether on the time scale relevant to the experiment (100 fs; see previous section), the evaluation of the nonlinear polarization according to the formalism of Sec. II gives expressions that are almost identical to the two-level results. The nonlinear polarization is still given by Eq. (18), only the system frequency ω_{ba} in the oscillating functions Ψ^A and Ψ^B of Eqs. (19) has to be modified.

The role of dephasing and/or rephasing processes is also identical to that in two-level systems. The apparent insignificance of vibrational dephasing on the time scales of interest amounts to a perfect correlation in the electronic fluctuations that occur on the optical transitions ω_{ba} and ω_{ca}. This is not unexpected. For instance, in gases and solids vibronic transitions generally have a correlated inhomogeneous width. This can be exploited in studies of dynamic behavior, since dephasing on one optical transition can be counteracted by rephasing on another one if memory is present in the dynamics [73–75]. The same is true here. Thus, in diagram I of Figs. 11(a) and 11(b) electronic dephasing and/or rephas-

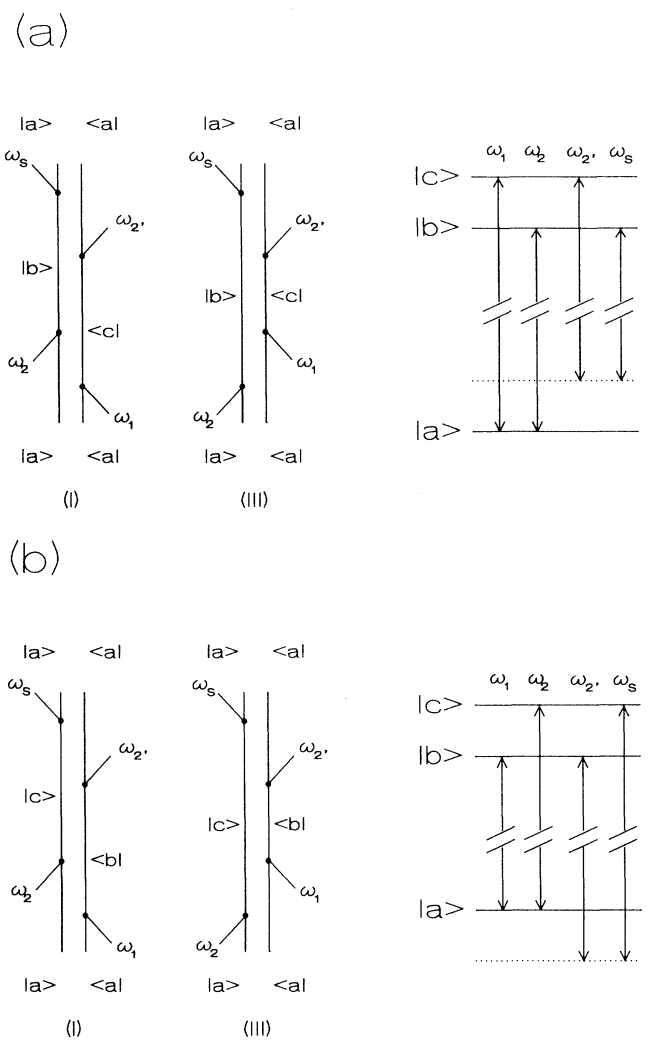

FIG. 11. Feynman diagrams and level scheme for three-level coherent Raman scattering. (a) The situation for coherent Stokes Raman scattering (CSRS). For positively chirped pulses ($\omega_2' \geq \omega_2$) a resonance occurs at positive delays ($\omega_1 > \omega_2$). (b) The corresponding situation for coherent anti-Stokes Raman scattering (CARS), which occurs at negative delays ($\omega_2 > \omega_1$). The diagrams are labeled I and III to allow for a direct comparison with the two-level diagrams of Fig. 3. With positive chirp the CSRS process can become fully resonant; for the CARS process this is only possible when the sign of the chirp is reversed ($\omega_2' \leq \omega_2$). For details see text.

ing processes are important, just as in diagrams I and II of Fig. 3, while in diagram III of Figs. 11(a) and 11(b) and diagrams III and IV of Fig. 3 rephasing cannot take place.

To calculate the system response for CSRS (positive delay) in the stochastic model, the terms $\omega_{ba}(t_3-t_1)$ and $\omega_{ba}(t_3+t_1)$ in the two-level oscillating functions $\Psi^{A,B}(t,\tau,t_3,t_2,t_1)$ of Eqs. (19) have to be replaced, respectively, by $\omega_{ba}t_3-\omega_{cb}t_2-\omega_{ca}t_1$ in Ψ^A (diagram I) and by $\omega_{ba}t_3-\omega_{cb}t_2+\omega_{ba}t_1$ in Ψ^B (diagram III). Similarly, these frequencies are in the case of CARS (negative delay) $\omega_{ca}t_3+\omega_{cb}t_2-\omega_{ba}t_1$ in Ψ^A (diagram I) and $\omega_{ca}t_3+\omega_{cb}t_2+\omega_{ca}t_1$ in Ψ^B (diagram III). The numerical evaluation of Eqs. (18)–(20) then proceeds along the same lines as described in Sec. IV for the two-level system.

Figure 12 shows how the calculated signal compares to the experimental trace. The dots in the upper curve relate to the three-level system. It is clear that the experimental trace is not as broad as the calculated one. We return to this point in the following section. The dynamic parameters used are identical to those of the previous calculations. The shape of the CARS signal that should be present at a delay of $\tau=-200$ fs is similar, but the calculated intensity is about a factor of 25 lower. This agrees with the experiment where no CARS signal is detectable above the noise level of the traces shown. Although it might be expected from Fig. 11 that the enhancement due to the difference frequency is symmetric for positive and negative delays, it is the direction of the chirp that causes the CARS signals to be much weaker than the CSRS signals.

The third interaction in the nonlinear process is for both CARS and CSRS induced by the field frequency ω_2', as depicted in the level structure of Fig. 11. Since the chirp is positive, frequency ω_2' is always larger than frequency ω_2. This means that in case of CSRS the finite chirp rate sweeps this interaction towards the resonance at ω_{ca}. An important point is that the state of the system before the third interaction is a vibrational coherence that shows dynamics on much longer time scales than is relevant to the experiment. Thus, the time t_2 in the Feynman diagrams of Fig. 11 can reach large values without damping playing any role. If t_2 increases substantially, ω_2' becomes much larger than ω_2, and therefore the enhancement of this part of the nonlinear process is considerable, due to resonance at ω_{ca}. However, this is only the case when the chirp of the pulses is positive.

From Fig. 11(b) it is clear that the frequency ω_2' is swept further from resonance when CARS instead of CSRS is generated with positively chirped pulses. As a result the CARS signals are considerably weaker than the corresponding CSRS signals. When the direction of the chirp is reversed, the opposite happens: CARS signals are then much stronger than CSRS signals, since now they are the ones that are swept into multiple enhancement by the chirped character of the optical fields.

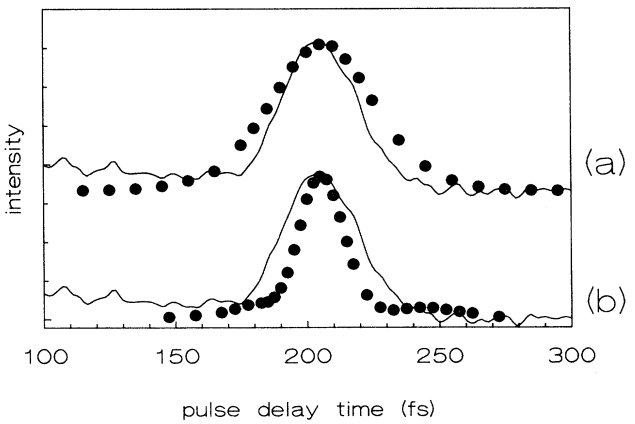

FIG. 12. Comparison of calculated and experimental chirped CSRS signals of resorufin in dimethylsulfoxide. The calculations (dots) are for stochastic frequency fluctuations with the parameter values of Fig. 4 in a three-level system (a), and in a four-level system with identical vibrational frequencies in electronic ground and excited states (b). The experimental result is identical to that of Fig. 10(a).

B. Four-level systems

As stated before, resorufin is better described by a four-level system than by a three-level system. The introduction of a fourth level, in the electronic ground state, leads to a number of new resonances. Additional Feynman diagrams are therefore required to fully describe chirped four-wave mixing in such a system. For positively chirped pulses the number of independent, fully resonant contributions in the case of CSRS is eight; four of these involve an excited-state vibrational resonance and four a ground-state one. In the case of CARS there is only one fully resonant Feynman diagram, which is propagated through the ground-state vibrational resonance.

The calculated response is given in the form of dots in the lower curve of Fig. 12. Due to the much larger number of quantum-mechanical pathways, the CSRS signal is much stronger for positively chirped pulses than the corresponding CARS signal. For negatively chirped pulses the situation is again reversed: CARS (eight fully resonant diagrams) is substantially stronger than CSRS (three fully resonant diagrams). Details on these more complicated chirped coherent Raman signals will be published elsewhere [76]. The general picture of Raman resonances that occur when the difference between the instantaneous frequencies of the fields match a system frequency remains the same, though.

Finally, we wish to comment on the discrepancy between the calculated and observed width of the CSRS signal. In the calculation we assumed that the ground- and excited-state vibrational frequencies are identical. This is not necessarily the case. Of course, it is possible to take the frequency difference as a parameter, which can be fitted by comparison with the experiment. The calculated curve will be broader then [76]. From the fact that the width in the three-level calculation is too large, we can conclude that such a level scheme is too simple to describe the relevant vibrational dynamics of resorufin.

The theoretical treatment of chirped coherent Raman

scattering given here is easily extended to deal with systems with more vibrational levels. Thus, the chirped coherent Raman signals provide direct and unequivocal information on the vibrational energies and vibronic intensities in electronic ground and excited states of complicated multilevel systems.

VI. CONCLUSIONS

We have shown that the grating-scattering type of experiment using linearly chirped excitation pulses can yield unique information on the dynamics of a system. Especially the question of whether or not the bath dynamics is determined by slow and fast fluctuations can be answered by simple inspection of the symmetry of the signal near zero delay time. Quantitative information from these four-wave-mixing experiments can only be obtained from numerical evaluation of third-order expressions for the induced polarization, and by assuming a specific model for the system dynamics.

As an example results of chirped scattering experiments and simulations of the signal, based on a stochastic model for the system dynamics, were presented on the system resorufin dissolved in dimethylsulfoxide. Excellent agreement is obtained between the calculations and the experiment when the bath parameters are used that were determined from impulsive photon-echo experiments on the same system. Apparently optical memory is already insignificant in this system on a 100-fs time scale.

It was further shown that in chirped four-wave mixing also coherent Raman signals are generated, which can be used to determine vibrational frequencies in the ground and excited states of molecules. For resorufin in dimethylsulfoxide the coherent Stokes Raman signal is shown to dominate the response. This is in agreement with numerical calculations of this effect. However, the calculations also show that for pulses with a reversed direction of the chirp the corresponding coherent anti-Stokes signals are much stronger. With the rapid advancements in femtosecond technology, the use of chirped four-wave mixing may become an important tool to probe vibrational dynamics of molecules in condensed phases.

ACKNOWLEDGMENTS

The investigations were supported by the Netherlands Foundations for Chemical Research (SON) and Physical Research (FOM) with financial aid from the Netherlands Organization for the Advancement of Science (NWO).

APPENDIX: BROWNIAN OSCILLATORS

The assumption that dynamics due to the coupling of a system with a bath can be described by the stochastic model of frequency fluctuations basically amounts to a high-temperature limit: upon excitation of the system the bath does not notice any difference in the interaction with the system. In a strict sense, this assumption is only warranted when the thermal energy of the bath is much larger than the excitation energy of the system. Of course, for optical excitations at room temperature such a high-temperature limit does not apply. The bath may react then to a change of state of the system, for instance by relaxing to an average configuration that is energetically more favorable.

A model that can take account of energy relaxation within an electronic state is that of the (multimode-) Brownian oscillator [63,77–79]. In this model the electronic two-level system is dressed with one (or more) harmonic mode(s) of the bath. The potential in which such an oscillator moves is assumed to be identical in both electronic states, but its equilibrium position is shifted. Therefore, upon a transition from one electronic state to another, according to the Condon principle the new equilibrium cannot be reached directly. This leads to a time dependence of the average energy of a state, so the propagators $\langle G_{aa}(t)\rangle$ and $\langle G_{bb}(t)\rangle$ of the Feynman diagrams of Fig. 3 differ now in more than just the population decay rates γ_a and γ_b.

Of special interest here is the case of an overdamped mode, which displays diffusive motion, and which can be characterized by an exponential correlation function [such as Eq. (9) for the stochastic model]. Such an overdamped mode does not necessarily represent a real excitation, but can also be considered as an abstract degree of freedom on which the non-Markovian characteristics of the bath are projected [63,78]. The basic propagator has the same form as in the stochastic model [Eq. (10)], but the damping function $g(t)$ is not given now by Eq. (11). Next to the real part an imaginary term appears:

$$g(t)=(\Delta^2/\Lambda^2)(e^{-\Lambda t}+\Lambda t-1)+i(\lambda/\Lambda)(1-e^{-\Lambda t}) . \tag{A1}$$

The reorganization parameter λ is related to the variance of the displacement Δ. In the high-temperature limit for the oscillator ($kT \gg \hbar\omega_0$) this relation is given by $\lambda \simeq \hbar\Delta^2/2kT$, which means that Eq. (A1) at a given temperature is determined by two parameters: Δ and Λ. Although the starting points are completely different, the result thus obtained in the Brownian oscillator model reads like a straightforward extension of the stochastic model. If the imaginary part of Eq. (A1) is negligible, the damping function is identical to that of the stochastic model.

When the imaginary part of the line-broadening function cannot be ignored, the propagation in ground ($|a\rangle\langle a|$) and excited ($|b\rangle\langle b|$) states is different. The system-bath dynamical functions $\Phi^A(t_3,t_2,t_1)$ and $\Phi^B(t_3,t_2,t_1)$ of Eqs. (14) then split to yield four different expressions for all diagrams I–IV of Fig. 3. In terms of the damping function $g(t)$ of Eq. (A1) the result is [63,77–79]

$$\Phi^{\mathrm{I}}(t_3,t_2,t_1)=g^*(t_3)+g^*(t_1)-g(t_2)+g(t_3+t_2) +g^*(t_2+t_1)-g^*(t_3+t_2+t_1) , \tag{A2a}$$

$$\Phi^{\mathrm{II}}(t_3,t_2,t_1)=g(t_3)+g^*(t_1)-g^*(t_2)+g^*(t_3+t_2) +g^*(t_2+t_1)-g^*(t_3+t_2+t_1) , \tag{A2b}$$

$$\Phi^{\mathrm{III}}(t_3,t_2,t_1)=g^*(t_3)+g(t_1)+g^*(t_2)-g^*(t_3+t_2) -g(t_2+t_1)+g(t_3+t_2+t_1)\ , \quad \text{(A2c)}$$

$$\Phi^{\mathrm{IV}}(t_3,t_2,t_1)=g(t_3)+g(t_1)+g(t_2)-g(t_3+t_2) -g(t_2+t_1)+g(t_3+t_2+t_1)\ . \quad \text{(A2d)}$$

When $\Phi^{\mathrm{I-IV}}$ [Eqs. (A2a)–(A2d)] are used instead of $\Phi^{A,B}$ [Eqs. (14)] for the nonlinear relaxation functions $R_{\mathrm{I-IV}}$ of Eqs. (13), the chirped nonlinear polarization equation (18) is modified as well. The calculation is straightforward. The numerical result that was presented in Fig. 8 for the Brownian oscillator model is calculated in this way.

[1] P. K. McGregor, Biol. Rev. Cambridge Philos. Soc. **66**, 57 (1991).

[2] N. Suga, Sci. Am. **262** (June), 34 (1990).

[3] J. R. Klauder, A. C. Price, S. Darlington, and W. J. Albersheim, Bell. Syst. Tech. J. **39**, 745 (1960).

[4] J.-C. Diels, W. Dietel, J. J. Fontaine, W. Rudolph, and B. Wilhelmi, J. Opt. Soc. B **2**, 680 (1985).

[5] M. A. Duguay and J. W. Hansen, Appl. Phys. Lett. **14**, 14 (1969).

[6] H. Nakatsuka, D. Grischkowsky, and A. C. Balant, Phys. Rev. Lett. **47**, 910 (1981).

[7] E. B. Treacy, IEEE J. Quantum Electron. **QE-5**, 454 (1969).

[8] R. L. Fork, O. E. Martinez, and J. P. Gordon, Opt. Lett. **9**, 150 (1984).

[9] D. Grischkowsky and A. C. Balant, Appl. Phys. Lett. **41**, 1 (1982).

[10] W. J. Tomlinson, R. H. Stolen, and C. V. Shank, J. Opt. Soc. Am. B **1**, 139 (1984).

[11] R. L. Fork, C. H. Brito Cruz, P. C. Becker, and C. V. Shank, Opt. Lett. **12**, 483 (1987).

[12] L. F. Mollenauer, J. P. Gordon, and M. N. Islam, IEEE J. Quantum Electron. **QE-22**, 157 (1986).

[13] P. Maine, D. Strickland, P. Bado, M. Pessot, and G. Mourou, IEEE J. Quantum Electron. **QE-24**, 398 (1988).

[14] S. Chelkowski, A. D. Bandrauk, and P. B. Corkum, Phys. Rev. Lett. **65**, 2355 (1990).

[15] B. Just, J. Manz, and I. Trisca, Chem. Phys. Lett. **193**, 423 (1992).

[16] J. S. Melinger, S. R. Gandhi, A. Hariharan, J. X. Tull, and W. S. Warren, Phys. Rev. Lett. **68**, 2000 (1992).

[17] B. Broers, H. B. van Linden van den Heuvel, and L. D. Noordam, Phys. Rev. Lett. **69**, 2062 (1992).

[18] T. Tokizaki, Y. Ishida, and T. Yajima, Opt. Commun. **71**, 355 (1989).

[19] E. T. J. Nibbering, D. A. Wiersma, and K. Duppen, Phys. Rev. Lett. **68**, 514 (1992).

[20] I. Burghardt, J.-M. Böhlen, and G. Bodenhausen, J. Chem. Phys. **93**, 7687 (1990).

[21] P. C. Becker, H. L. Fragnito, J.-Y. Bigot, C. H. Brito Cruz, R. L. Fork, and C. V. Shank, Phys. Rev. Lett. **63**, 505 (1989).

[22] E. T. J. Nibbering, D. A. Wiersma, and K. Duppen, Phys. Rev. Lett. **66**, 2464 (1991).

[23] J.-Y. Bigot, M. T. Portella, R. W. Schoenlein, J. E. Cunningham, and C. V. Shank, Phys. Rev. Lett. **67**, 636 (1991).

[24] S. Weiss, M. A. Mycek, J.-Y. Bigot, S. Schmitt-Rink, and D. S. Chemla, Phys. Rev. Lett. **69**, 2685 (1992).

[25] T. Yajima and H. Souma, Phys. Rev. A **17**, 309 (1978).

[26] R. Trebino, C. E. Barker, and A. E. Siegman, IEEE J. Quantum Electron. **QE-22**, 1413 (1986).

[27] S. Asaka, H. Nakatsuka, M. Fujiwara, and M. Matsuoka, Phys. Rev. A **29**, 2286 (1984).

[28] N. Morita and T. Yajima, Phys. Rev. A **30**, 2525 (1984).

[29] W. H. Knox, Opt. Photonics News **3** (May), 10 (1992).

[30] T. K. Yee and T. K. Gustafson, Phys. Rev. A **18**, 1597 (1978).

[31] P. Ye and Y. R. Shen, Phys. Rev. A **25**, 2183 (1982).

[32] J. G. Fujimoto and T. K. Yee, IEEE J. Quantum Electron. **QE-19**, 861 (1983).

[33] S. Mukamel and R. F. Loring, J. Opt. Soc. Am. B **3**, 595 (1986).

[34] P. W. Anderson and P. R. Weiss, Rev. Mod. Phys. **25**, 269 (1953).

[35] R. Kubo, Adv. Chem. Phys. **15**, 101 (1969).

[36] T. Takagahara, E. Hanamura, and R. Kubo, J. Phys. Soc. Jpn. **43**, 802 (1977); **43**, 811 (1977); **43**, 1522 (1977).

[37] M. Aihara, Phys. Rev. B **25**, 53 (1982).

[38] H. Risken, *The Fokker-Planck Equation* (Springer-Verlag, Berlin, 1984).

[39] E. T. J. Nibbering, D. A. Wiersma, and K. Duppen, in *Coherence in Atoms and Molecules in Laser Fields,* Vol. 287 of *NATO Advanced Study Institute, Series B: Physics,* edited by A. D. Bandrauk and S. C. Wallace (Plenum, New York, 1992), p. 377.

[40] M. C. Wang and G. E. Uhlenbeck, Rev. Mod. Phys. **17**, 323 (1945).

[41] J. R. Klauder and P. W. Anderson, Phys. Rev. **125**, 912 (1962).

[42] R. Kubo, in *Fluctuation, Relaxation and Resonance in Magnetic Systems,* edited by D. ter Haar (Oliver and Boyd, London, 1962), p. 23.

[43] S. Mukamel, Phys. Rev. A **28**, 3480 (1983).

[44] F. Bloch, Phys. Rev. **70**, 460 (1946).

[45] L. Allen and J. H. Eberly, *Optical Resonance and Two-Level Atoms* (Wiley, New York, 1975).

[46] A limiting form of the delta function is $\delta(t)=\lim_{b\to\infty}\sqrt{b/2\pi}e^{-bt^2/2}$.

[47] B. D. Fainberg, Opt. Spektrosk. **55**, 1098 (1983) [Opt. Spectrosc. (USSR) **55**, 669 (1983)].

[48] R. F. Loring and S. Mukamel, Chem. Phys. Lett. **114**, 426 (1985).

[49] K.-E. Süsse, W. Vogel, and D.-G. Welsch, Chem. Phys. Lett. **162**, 287 (1989).

[50] S. Mukamel, J. Chem. Phys. **82**, 5398 (1985).

[51] Y. Tanimura, and R. Kubo, J. Phys. Soc. Jpn. **58**, 101 (1989).

[52] Equation (9) in Ref. [25]; note that the signal is calculated for the direction $2\mathbf{k}_1-\mathbf{k}_2$ in that case.

[53] P. J. Davis and P. Rabinowitz, *Methods of Numerical Integration* (Academic, New York, 1975).

[54] W. H. Press, B. P. Flannery, S. A. Teukolsky, and W. T. Vetterling, *Numerical Recipes* (Cambridge Univ. Press, Cambridge, 1986).

[55] Routine D01gbf, NAG Fortran Library Manual (mark 14), Numerical Algorithms Group, 1989.

[56] Y. S. Bai and T. W. Mossberg, Appl. Phys. Lett. **45**, 1269 (1984).

[57] J. E. Rothenberg and D. Grischkowsky, J. Opt. Soc. Am. B **2**, 626 (1985).

[58] J. E. Rothenberg, IEEE J. Quantum Electron. **QE-22**, 174 (1986).
[59] When population relaxation is taken into account, the integrals do converge, but at unrealistically high values. The argument of interference between diagrams remains valid.
[60] P. F. Barbara and W. Jarzeba, Adv. Photochem. **15**, 1 (1990).
[61] S. J. Rosenthal, X. Xie, M. Du, and G. R. Fleming, J. Chem. Phys. **95**, 4715 (1991).
[62] E. T. J. Nibbering, K. Duppen, and D. A. Wiersma, J. Photochem. Photobiol. A: Chem. **62**, 347 (1992).
[63] D.A. Wiersma, E. T. J. Nibbering, and K. Duppen, in *Ultrafast Phenomena VIII,* edited by J. L. Martin, A. Migus, G. A. Mourou, and A. H. Zewail, Springer Series in Chemical Physics (Springer-Verlag, Berlin, in press).
[64] This follows from $\lim_{l\to\infty}\int_{-l}^{+l}e^{i\omega t}d\omega=\delta(t)$ in Eq. (33) with the polarization given by Eq. (18) and with the variables $t_{1,2,3}$ defined to be positive.
[65] T. Yajima, H. Souma, and Y. Ishida, Phys. Rev. A **17**, 324 (1978).
[66] H. Souma, E. J. Heilweil, and R. M. Hochstrasser, J. Chem. Phys. **76**, 5693 (1982).
[67] J.-Y. Bigot, M. T. Portella, R. W. Schoenlein, C. J. Bardeen, A. Migus, and C. V. Shank, Phys. Rev. Lett. **66**, 1138 (1991).
[68] M. Cho, S. J. Rosenthal, N. F. Scherer, L. D. Ziegler, and G. R. Fleming, J. Chem. Phys. **96**, 5033 (1992).
[69] Y. Prior, A. R. Bogdan, M. Dagenais, and N. Bloembergen, Phys. Rev. Lett. **46**, 111 (1981).
[70] J. R. Andrews and R. M. Hochstrasser, Chem. Phys. Lett. **83**, 427 (1981).
[71] J. R. Andrews, R. M. Hochstrasser, and H. P. Trommsdorff, Chem. Phys. **62**, 87 (1981).
[72] D. P. Weitekamp, K. Duppen, and D. A. Wiersma, Phys. Rev. A **27**, 3089 (1983).
[73] T. W. Mossberg, A. M. Flusberg, R. Kachru, and S. R. Hartmann, Phys. Rev. Lett. **42**, 1665 (1979).
[74] K. Duppen, D. P. Weitekamp, and D. A. Wiersma, Chem. Phys. Lett. **106**, 147 (1984).
[75] K. Duppen, D. P. Weitekamp, and D. A. Wiersma, Chem. Phys. Lett. **108**, 551 (1984).
[76] E. T. J. Nibbering, F. de Haan, D. A. Wiersma, and K. Duppen (unpublished).
[77] Y. J. Yan and S. Mukamel, J. Chem. Phys. **89**, 5160 (1988).
[78] Y. J. Yan and S. Mukamel, Phys. Rev. A **41**, 6485 (1990).
[79] Y. J. Yan and S. Mukamel, J. Chem. Phys. **93**, 3863 (1991).